

Article

Not peer-reviewed version

Complex Photonic Integrated Resonators Modeled Using Scattering Matrix Methods

[David Moss](#)*

Posted Date: 8 October 2024

doi: 10.20944/preprints202410.0477.v1

Keywords: integrated photonics; scattering matrix method; microring resonators



Preprints.org is a free multidiscipline platform providing preprint service that is dedicated to making early versions of research outputs permanently available and citable. Preprints posted at Preprints.org appear in Web of Science, Crossref, Google Scholar, Scilit, Europe PMC.

Copyright: This is an open access article distributed under the Creative Commons Attribution License which permits unrestricted use, distribution, and reproduction in any medium, provided the original work is properly cited.

Article

Complex Photonic Integrated Resonators Modeled Using Scattering Matrix Methods

David J. Moss ^{1,2}

¹ Optical Sciences Centre, Swinburne University of Technology, Hawthorn, Victoria 3122, Australia; dmoss@swin.edu.au

² The ARC Centre of Excellence in Optical Microcombs for Breakthrough Science (COMBS), Melbourne 3000, Victoria, Australia

Abstract: We propose a universal approach for modeling complex integrated photonic resonators based on the scattering matrix method. By dividing devices into basic elements including directional couplers and connecting waveguides, our approach can be used to model integrated photonic resonators with both unidirectional and bidirectional light propagation, with the simulated spectral response showing good agreement with experimental results. A simplified form of our approach, which divides devices into several independent submodules such as microring resonators and Sagnac interferometers, is also introduced to streamline the calculation of spectral transfer functions. Finally, we discuss the deviations introduced by approximations in our modeling, along with strategies for improving modeling accuracy. Our approach is universal across different integrated platforms, providing a useful tool for designing and optimizing integrated photonic devices with complex configurations.

Keywords: integrated photonics; scattering matrix method; microring resonators

1. Introduction

With compact footprint and versatile configuration, integrated photonic resonators have become critical building blocks for photonic integrated circuits (PICs), with applications in a wide range of fields such as optical communications [1–3], photonic computing [4–6], nonlinear optics [7–9], sensing [10–12], and optical neural networks [13–15].

Modeling the spectral response of integrated photonic resonators is of fundamental importance for their use in different applications. The scattering matrix method (SMM) (also known as the transfer matrix method) [16,17], which is derived based on the Maxwell's equations for electromagnetic waves, has been widely employed to model the spectral response of integrated photonic resonators with different device configurations [17–22].

Although in principle the SMM can be applied to model integrated photonic devices with arbitrary planar configurations [16,23], previous studies mainly focused on modeling devices with simple configurations. A key limitation comes from the fact that the traditional SMM relies on the manual derivation of scattering matrices, and the obtained scattering matrices need to be multiplied in a specific sequence [24]. For devices with simple configurations, this allows for relatively straightforward calculation of spectral transfer functions. However, for complex integrated photonic resonators, particularly those with bidirectional light propagation, this process becomes much more complicated, which greatly limits its broader applicability.

In this paper, a universal approach based on the SMM is proposed to model integrated photonic resonators with complex structures. The modeling is achieved by dividing a device configuration into basic elements including directional couplers and connecting waveguides, followed by solving a system of linear scattering matrix equations using computational tools. Our approach can be applied to model devices with both unidirectional and bidirectional light propagation, and the simulated spectral response aligns well with measured results for practical devices. The modeling in

our approach can also be simplified by dividing the device configuration into independent submodules such as microring resonators (MRRs) and Sagnac interferometers (SIs). Finally, we discuss the limitations of our approach induced by approximations in the modeling, together with strategies for improving modeling accuracy. Our approach provides an effective way for designing and optimizing complex integrated photonic devices across various integrated platforms.

2. Modeling of Devices with Unidirectional Light Propagation

In this section, we use the device configuration shown in **Figure 1(a)** as an example to show how to model a complex integrated photonic resonator based on the SMM in four steps. The device consists of a microring resonator (MRR) nested within another, with light propagating in only one direction in each waveguide.

First, we divide the device into several directional couplers and connecting waveguides, which are the basic elements in photonic integrated circuits that form integrated photonic resonators. The optical fields at the dividing points between these elements are denoted as E_i ($i = 1-16$).

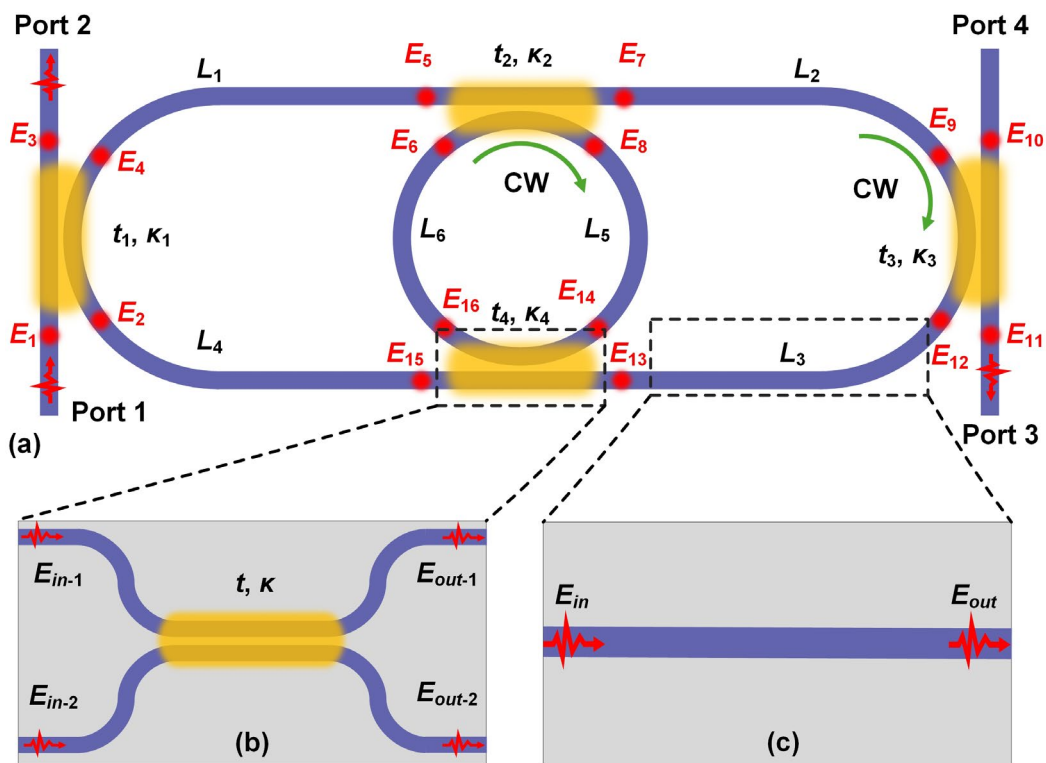


Figure 1. (a) Schematic illustration of an integrated photonic resonator consisting of two microring resonators (MRRs) with an input from Port 1. The device is divided into several directional couplers and connecting waveguides, with E_i ($i = 1-16$) denoting the optical fields at the dividing points. (b) – (c) zoom-in views for a directional coupler and a connecting waveguide, respectively.

Next, we establish a set of scattering matrix equations for the basic elements obtained in the first step, as shown in **Table 1**. These scattering matrix equations describe the relation between E_i at the input / output ports of the directional couplers and the connecting waveguides. For the directional coupler in **Figure 1(b)**, the field transfer function can be expressed as [16]

$$\begin{bmatrix} E_{out-1} \\ E_{out-2} \end{bmatrix} = \begin{bmatrix} t & j\kappa \\ j\kappa & t \end{bmatrix} \begin{bmatrix} E_{in-1} \\ E_{in-2} \end{bmatrix}, \quad (1)$$

where $j = \sqrt{-1}$, t and κ are the self-coupling and cross coupling coefficients, which satisfies the relation $t^2 + \kappa^2 = 1$ when assuming lossless coupling, E_{in-1} , E_{in-2} , E_{out-1} , and E_{out-2} are the input and output optical fields right before and after the coupling region. For the connecting waveguide in **Figure 1(c)**, the field transfer function can be given by [23]

$$T = ae^{j\varphi}, \quad (2)$$

where $a = e^{-\alpha L/2}$ is the round-trip transmission factor, with α and L denoting the power propagation loss factor and the waveguide length, respectively. In Eq. (2), $\varphi = 2\pi n_g L/\lambda$ is the round-trip phase shift, with n_g and λ denoting the group index and the wavelength, respectively. For each directional coupler, two equations can be derived, and one equation can be obtained for each connecting waveguide. This results in $2 \times 4 + 1 \times 6 = 14$ equations in total for the device shown in Figure 1(a), which includes four directional couplers and six connecting waveguides.

Table 1. Definitions of structural parameters of the device in Figure 1(a) and the corresponding scattering matrix equations.

| | Structural Parameters ($i = 1 - 4$) | Field transmission coefficient t_i | Field cross coupling coefficient κ_i | |
|------------------------------|--|--|---|----------------------------|
| Directional couplers | Scattering matrix equations | $\begin{bmatrix} E_3 \\ E_4 \end{bmatrix} = \begin{bmatrix} t_1 & j\kappa_1 \\ j\kappa_1 & t_1 \end{bmatrix} \begin{bmatrix} E_1 \\ E_2 \end{bmatrix}'$ $\begin{bmatrix} E_{12} \\ E_{11} \end{bmatrix} = \begin{bmatrix} t_3 & j\kappa_3 \\ j\kappa_3 & t_3 \end{bmatrix} \begin{bmatrix} E_9 \\ E_{10} \end{bmatrix}'$ | $\begin{bmatrix} E_7 \\ E_8 \end{bmatrix} = \begin{bmatrix} t_2 & j\kappa_2 \\ j\kappa_2 & t_2 \end{bmatrix} \begin{bmatrix} E_5 \\ E_6 \end{bmatrix}'$ $\begin{bmatrix} E_{15} \\ E_{16} \end{bmatrix} = \begin{bmatrix} t_4 & j\kappa_4 \\ j\kappa_4 & t_4 \end{bmatrix} \begin{bmatrix} E_{13} \\ E_{14} \end{bmatrix}'$ | |
| | Structural Parameters ($i = 1 - 6$) | Length L_i | Transmission factor a_i | Phase shift φ_i |
| Connecting waveguides | Scattering matrix equations | | $E_5 = T_1 E_4, E_9 = T_2 E_7, E_{13} = T_3 E_{12},$ $E_2 = T_4 E_{15}, E_{14} = T_5 E_8, E_6 = T_6 E_{16}.$ | |
| Input | | $E_1 = 1, E_{10} = 0.$ | | |

Third, the system input is set. For instance, if we assume that there is only a continuous-wave (CW) input from Port 1, then another two equations can be obtained: $E_1 = 1$ and $E_{10} = 0$. Here we set E_1 as 1 because the spectral transfer function at the output port, such as Port 2, is given by $f_{\text{Port 2}} = E_3 / E_1$. By setting E_1 to 1, $f_{\text{Port 2}} = E_3 / E_1 = E_3$, then the transfer function can be directly determined by calculating E_3 in the next step.

Finally, by solving all the linear equations obtained in the second and third steps, one can obtain the spectral transfer functions at the output ports. In Table 1, we summarize all the 16 equations for the device in Figure 1(a). In these equations, there are 16 variables E_i ($i = 1-16$), with the device's structural parameters denoted using symbols and treated as constant coefficients. By solving this system of linear equations using computational tools (e.g., symbolic calculation in MATLAB), any of the variables E_i ($i = 1-16$) can be determined as a function of the device's structural parameters. For example, the spectral transfer function at Port 2 can be given by $f_{\text{Port 2}} = E_3(T_i, t_i, \kappa_i)$. Assuming that the power propagation loss factor α and the group index n_g are constant for the device, the spectral transfer function at Port 2 can be expressed as a function of L_i, t_i , and κ_i , i.e., $f_{\text{Port 2}} = E_3(L_i, t_i, \kappa_i)$.

In Figure 2(a), we show the intensity and phase response spectra at Port 2 for different t_i based on the obtained spectral transfer function $f_{\text{Port 2}} = E_2(L_i, t_i, \kappa_i)$. Except for the varying parameters, other structural parameters were chosen as follows: $L_1 = L_2 = L_3 = L_4 = 41.73 \mu\text{m}$, $L_5 = L_6 = 62.83 \mu\text{m}$, and $t_2 = t_4 = 0.98$. By using the same method, we obtain the intensity and phase responses at Port 3 for different t_i , as shown in Figure 2(b). In our modeling, we assume that $\alpha = 101 \text{ m}^{-1}$ and group index $n_g = 4.335$ based on values obtained from our previously fabricated silicon photonic devices [20,25]. Unless otherwise specified, we use the same values for these two parameters in the modeling for all the devices in the following figures.

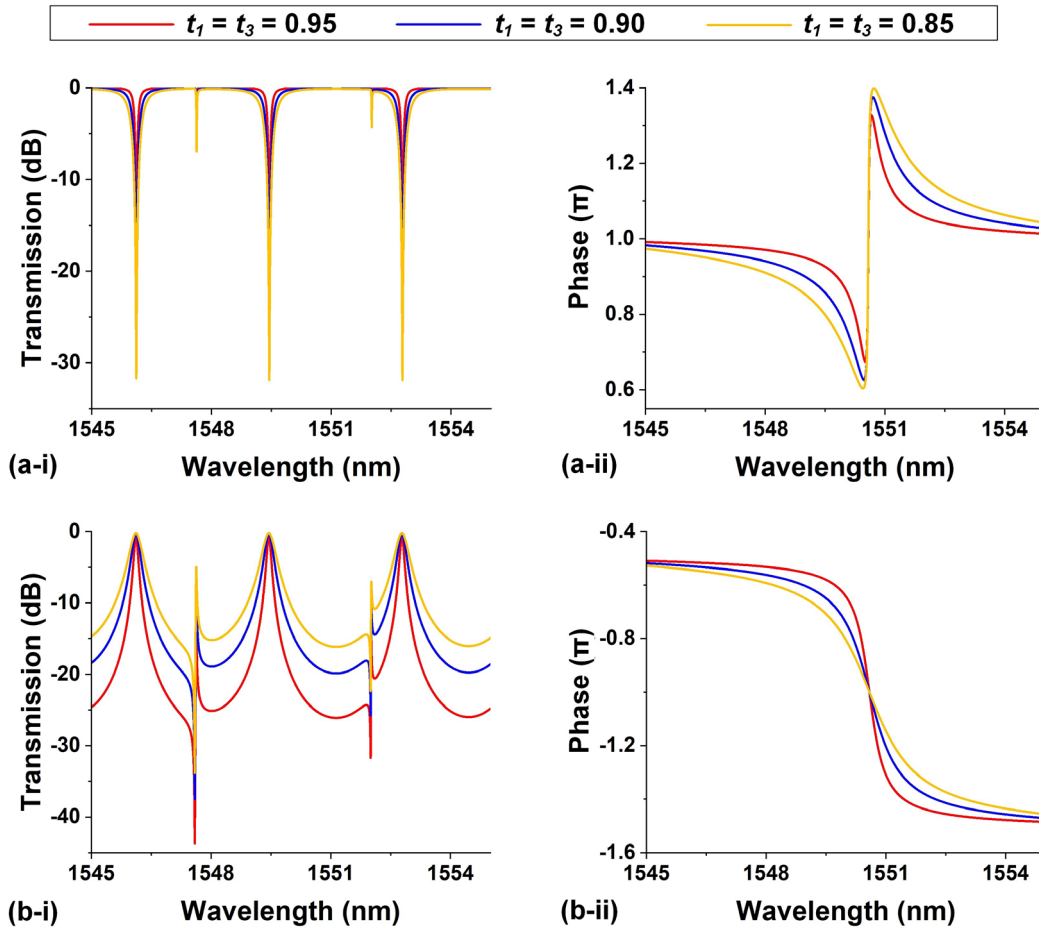


Figure 2. (a) Calculated (i) intensity and (ii) phase response spectra at Port 2 for the device in **Figure 1** with different $t_1 = t_3$. (b) Calculated (i) intensity and (ii) phase response spectra at Port 3 for the device in **Figure 1** with different $t_1 = t_3$. In (a) and (b), $t_2 = t_4 = 0.98$. The power propagation loss factor α and group index n_g are assumed to be 101 m^{-1} and 4.335, respectively.

Our results in **Figure 2** show good agreement with the results in Ref. [26], confirming the effectiveness of our method. Since the obtained spectral transfer functions (e.g., $f_{\text{Port } 2} = E_2(L_i, t_i, \kappa_i)$) include all the structural parameters, the intensity and phase responses can be easily tailored by adjusting any of these parameters. This provides significant flexibility in designing and optimizing the spectral response of integrated photonic devices with different structural parameters. It should also be noted that our modeling, as mentioned above, is not limited to silicon photonic platforms. By using the corresponding values of α and n_g , it is applicable across various integrated platforms such as silicon nitride, doped silica, and lithium niobate [27–93].

3. Modeling of Devices with Bidirectional Light Propagation

For the device in **Figure 1(a)**, light propagates in only one direction along each waveguide. In more complex integrated photonic resonators with light propagating bidirectionally in the waveguides, the modeling becomes more complicated. In this section, we use the device configuration shown in **Figure 3(a)** as an example to show how to model a complex integrated photonic resonator with bidirectional light propagation based on the SMM. The device consists of an add-drop (AD) MRR sandwiched between a pair of Sagnac interferometers (SIs), where the SIs introduce back reflection and hence bidirectional light propagation in such device.

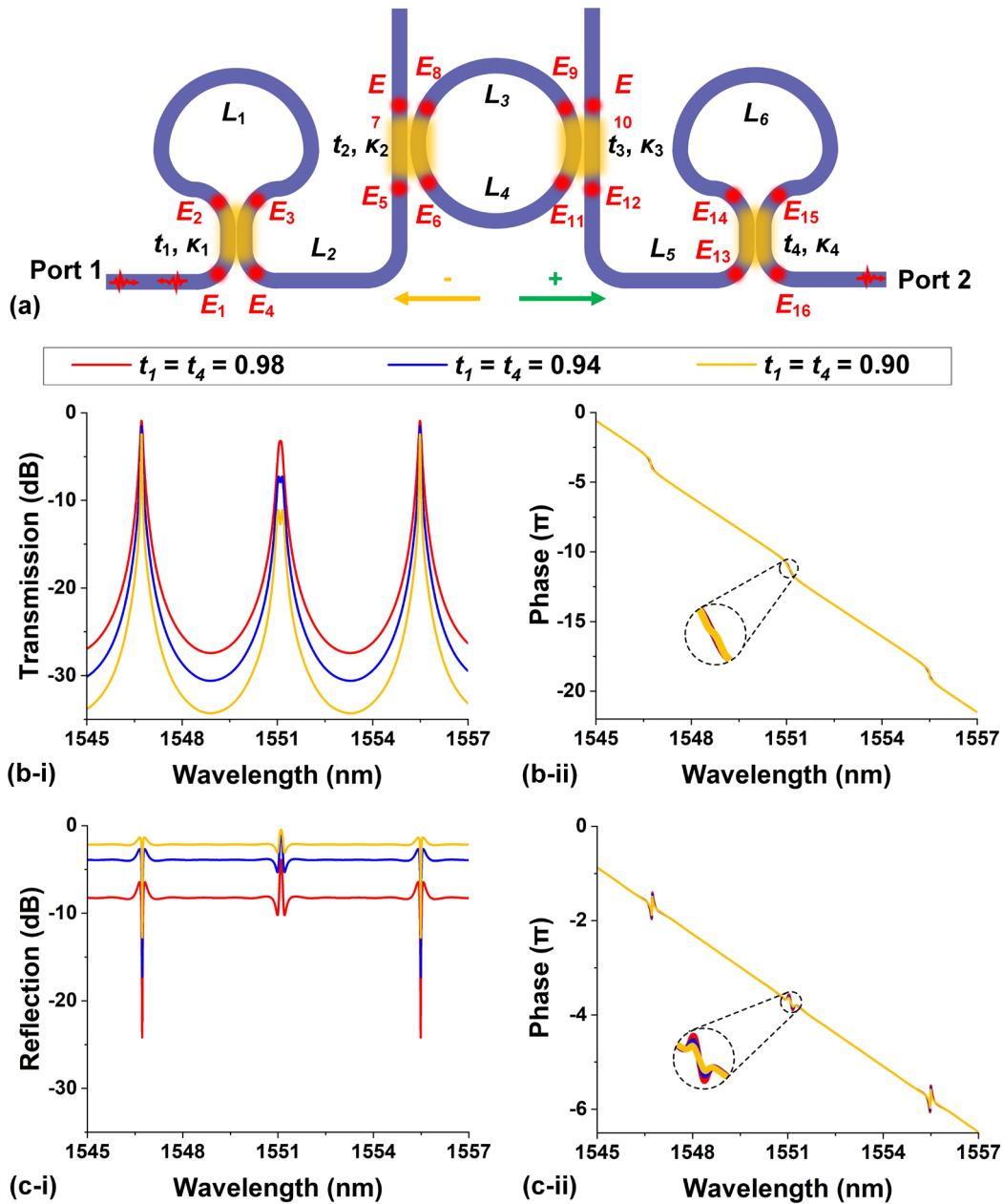


Figure 3. (a) Schematic illustration of an integrated photonic resonator formed by an add-drop micro-ring resonator (AD-MRR) sandwiched between two Sagnac interferometers (SIs) with an input from Port 1. The device is divided into several directional couplers and connecting waveguides, with E_i ($i = 1-16$) denoting the optical fields at the dividing points. The electric fields propagating from left to right are defined as "+" direction and the ones propagating from right to left are defined as "-" direction. (b) Calculated (i) power transmission and (ii) phase response spectra at Port 2 for different $t_1 = t_4$. (c) Calculated (i) power reflection and (ii) phase response spectra at Port 1 for different $t_1 = t_4$.

To model the device in Figure 3(a), we first divide it into several directional couplers and connecting waveguides – the same as what we did for the device in Figure 1(a). The optical fields at the dividing points between directional couplers and connecting waveguides are denoted as E_i ($i = 1-16$). Since there are optical fields traveling in two different directions at each dividing point, the optical fields traveling from left to right or in a clockwise direction are defined as "+", and the opposite direction is defined as "-".

In the second step, we establish 28 scattering matrix equations describing the relation between E_i^+ and E_i^- at the input / output ports of the directional couplers and the connecting waveguides, as shown in Table 2. For each directional coupler, four equations can be derived, and two equations can

be obtained for each connecting waveguide. Note that the number of equations is doubled due to the bidirectional light propagation in such device.

In the third step, we obtain another four equations by setting the system input. If we assume that there is only a CW input from Port 1, then the four equations are: $E_{1^+} = 1$, $E_{7^-} = 0$, $E_{10^+} = 0$, and $E_{16^-} = 0$. Here the number of equations is also doubled due to the bidirectional light propagation.

Finally, by solving all the 32 linear equations obtained previously (which include 32 variables, i.e., E_i^+ and E_i^- , $i = 1-16$), we can obtain the spectral transfer functions at all the output ports. For example, the transfer function for forward transmission, with output at Port 2, is $f_{\text{Port 2}} = E_{16^+}(L_i, t_i, \kappa_i)$, whereas the transfer function for backward reflection is $f_{\text{Port 1}} = E_{1^-}(L_i, t_i, \kappa_i)$, with output at Port 1. It should be noted that as the number of equations increases or the device configuration becomes more complex, the use of computational software to solve the system of linear equations offers significant advantages as compared to manual derivation of the spectral transfer functions as those in Refs. [25,26].

Table 2. Definitions of structural parameters of the device in Figure 3(a) and the corresponding scattering matrix equations.

| Structural Parameters ($i = 1 - 4$) | | Field transmission coefficient t_i | Field cross coupling coefficient κ_i | |
|--|---|--|--|---|
| Directional couplers | Scattering matrix equations | $\begin{bmatrix} E_2^+ \\ E_3^- \end{bmatrix} = \begin{bmatrix} t_1 & j\kappa_1 \\ j\kappa_1 & t_1 \end{bmatrix} \begin{bmatrix} E_1^+ \\ E_4^- \end{bmatrix}$ | $\begin{bmatrix} E_1^- \\ E_4^+ \end{bmatrix} = \begin{bmatrix} t_1 & j\kappa_1 \\ j\kappa_1 & t_1 \end{bmatrix} \begin{bmatrix} E_2^- \\ E_3^+ \end{bmatrix}$ | |
| | | $\begin{bmatrix} E_7^+ \\ E_8^- \end{bmatrix} = \begin{bmatrix} t_2 & j\kappa_2 \\ j\kappa_2 & t_2 \end{bmatrix} \begin{bmatrix} E_5^+ \\ E_6^- \end{bmatrix}$ | $\begin{bmatrix} E_5^- \\ E_6^+ \end{bmatrix} = \begin{bmatrix} t_2 & j\kappa_2 \\ j\kappa_2 & t_2 \end{bmatrix} \begin{bmatrix} E_7^- \\ E_8^+ \end{bmatrix}$ | |
| | | $\begin{bmatrix} E_{11}^+ \\ E_{12}^- \end{bmatrix} = \begin{bmatrix} t_3 & j\kappa_3 \\ j\kappa_3 & t_3 \end{bmatrix} \begin{bmatrix} E_9^+ \\ E_{10}^- \end{bmatrix}$ | $\begin{bmatrix} E_9^- \\ E_{10}^+ \end{bmatrix} = \begin{bmatrix} t_3 & j\kappa_3 \\ j\kappa_3 & t_3 \end{bmatrix} \begin{bmatrix} E_{11}^- \\ E_{12}^+ \end{bmatrix}$ | |
| | | $\begin{bmatrix} E_{14}^+ \\ E_{15}^- \end{bmatrix} = \begin{bmatrix} t_4 & j\kappa_4 \\ j\kappa_4 & t_4 \end{bmatrix} \begin{bmatrix} E_{13}^+ \\ E_{16}^- \end{bmatrix}$ | $\begin{bmatrix} E_{13}^- \\ E_{16}^+ \end{bmatrix} = \begin{bmatrix} t_4 & j\kappa_4 \\ j\kappa_4 & t_4 \end{bmatrix} \begin{bmatrix} E_{14}^- \\ E_{15}^+ \end{bmatrix}$ | |
| Structural Parameters ($i = 1 - 6$) | Length L_i | Transmission factor a_i | Phase shift φ_i | |
| Connecting waveguides | Scattering matrix equations | $\begin{bmatrix} E_3^+ \\ E_2^- \end{bmatrix} = T_1 \begin{bmatrix} E_2^+ \\ E_3^- \end{bmatrix}$ | $\begin{bmatrix} E_5^+ \\ E_4^- \end{bmatrix} = T_2 \begin{bmatrix} E_4^+ \\ E_5^- \end{bmatrix}$ | $\begin{bmatrix} E_9^+ \\ E_8^- \end{bmatrix} = T_3 \begin{bmatrix} E_8^+ \\ E_9^- \end{bmatrix}$ |
| | | $\begin{bmatrix} E_6^+ \\ E_{11}^- \end{bmatrix} = T_4 \begin{bmatrix} E_{11}^+ \\ E_6^- \end{bmatrix}$ | $\begin{bmatrix} E_{13}^+ \\ E_{12}^- \end{bmatrix} = T_5 \begin{bmatrix} E_{12}^+ \\ E_{13}^- \end{bmatrix}$ | $\begin{bmatrix} E_{15}^+ \\ E_{14}^- \end{bmatrix} = T_6 \begin{bmatrix} E_{14}^+ \\ E_{15}^- \end{bmatrix}$ |
| Input | $E_{1^+} = 1, E_{7^-} = 0, E_{10^+} = 0, E_{16^-} = 0.$ | | | |

Based on the obtained spectral transfer functions at Port 2 and Port 1, we plot the corresponding response spectra for different t_i , as shown in **Figures 3(b)** and **3(c)**, respectively. Except for t_i , the other structural parameters are kept as constant as: $L_1 = L_6 = 129.66 \mu\text{m}$, $L_2 = L_5 = 77.67 \mu\text{m}$, $L_3 = L_4 = 63.33 \mu\text{m}$, and $t_2 = t_3 = 0.95$. Our results in **Figure 3** also show good agreement with the results in Ref. [25], confirming the effectiveness of our method in modeling complex integrated photonic resonator with bidirectional light propagation.

4. Simplification by Dividing Device into Submodules

In modeling of the device configurations in **Figures 1(a)** and **3(a)**, the devices were divided into several basic elements including directional couplers and connecting waveguides. To reduce the number of equations and simplify the calculation of the spectral transfer function, the device configuration can also be divided into several independent submodules such as MRRs and SIs, which are formed by the basic elements.

As illustrated in **Figure 4(a)**, the AD-MRR at the center of the device in **Figure 1(a)** is treated as an independent module, with the field transfer functions at the through and drop ports denoted as T_{RR} and D_{RR} , respectively. This results in 12 equations in total obtained by using our method

mentioned previously, as summarized in **Table 3**. In comparison to the 16 equations obtained for the same device configuration in **Table 1**, the number of equations is reduced, which helps to simplify the solving of the system of equations. By solving the 12 equations in **Table 3**, the spectral transfer function at Port 2 can be obtained, which is a function of T_{MRR} and D_{MRR} . We compared the response spectra obtained by solving the equations in **Tables 1** and **3** and found them to be identical. This verifies the validity of the new dividing method in **Figures 4(a)**. It is also worth mentioning that when plotting the response spectra based on this dividing method, T_{MRR} and D_{MRR} should be further expressed as [94]

$$T_{RR} = \frac{E_6}{E_5} = \frac{E_{12}}{E_{11}} = \frac{t_{RR-1} - t_{RR-2}a_{RR}e^{j\varphi_{RR}}}{1 - t_{RR-1}t_{RR-2}a_{RR}e^{j\varphi_{RR}}}, \quad (3)$$

$$D_{RR} = \frac{E_{12}}{E_5} = \frac{E_6}{E_{11}} = \frac{-\kappa_{RR-1}\kappa_{RR-2}\sqrt{a_{RR}}e^{j\varphi_{RR}}}{1 - t_{RR-1}t_{RR-2}a_{RR}e^{j\varphi_{RR}}}, \quad (4)$$

where $j = \sqrt{-1}$, a_{RR} and φ_{RR} are the round-trip transmission factor and phase shift along the ring in the AD-MRR, respectively. t_{RR-i} and κ_{RR-i} ($i = 1, 2$) are the self-coupling and cross coupling coefficients of the directional couplers in the AD-MRR, respectively.

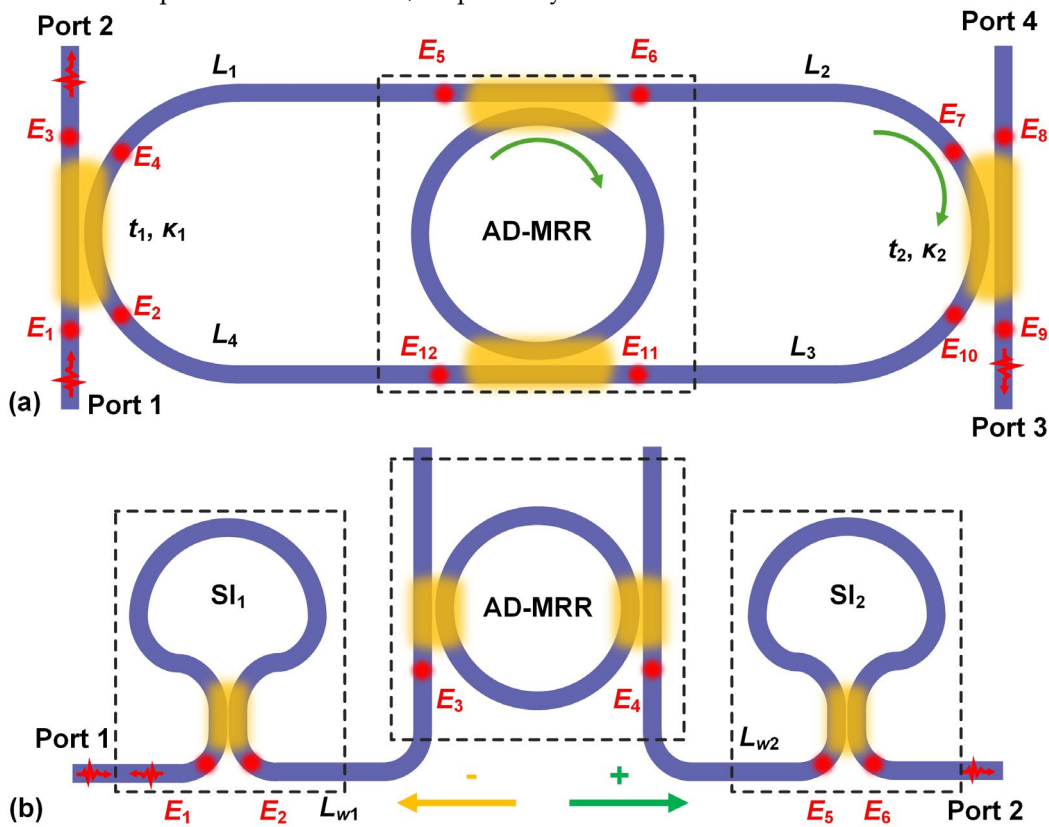


Figure 4. Dividing device configuration into submodules to simplify the calculation (a) Device configuration in **Figure 1(a)**, where the add-drop micro-ring resonator (AD-MRR) at the center is regarded as an independent module. (b) Device configuration in **Figure 3(a)**, which is divided into submodules including an AD-MRR, two Sagnac interferometers (SIs), and connecting waveguides between them.

Table 3. Scattering matrix equations for the device in **Figure 4(a)**. T_{RR} and D_{RR} are the field transfer functions at the through and drop ports for the AD-MRR, respectively.

| | | |
|-----------------------------|--|--|
| Scattering matrix equations | Add-drop micro-ring resonator (AD-MRR) | $\begin{bmatrix} E_6 \\ E_{12} \end{bmatrix} = \begin{bmatrix} T_{RR} & D_{RR} \\ D_{RR} & T_{RR} \end{bmatrix} \begin{bmatrix} E_5 \\ E_{11} \end{bmatrix}.$ |
| | Directional couplers | $\begin{bmatrix} E_3 \\ E_4 \end{bmatrix} = \begin{bmatrix} t_1 & j\kappa_1 \\ j\kappa_1 & t_1 \end{bmatrix} \begin{bmatrix} E_1 \\ E_2 \end{bmatrix}, \quad \begin{bmatrix} E_{10} \\ E_9 \end{bmatrix} = \begin{bmatrix} t_2 & j\kappa_2 \\ j\kappa_2 & t_2 \end{bmatrix} \begin{bmatrix} E_7 \\ E_8 \end{bmatrix}.$ |

| | |
|-----------------------|--|
| Connecting waveguides | $E_5 = T_{w1}E_4, E_7 = T_{w2}E_6, E_{11} = T_{w3}E_{10}, E_2 = T_{w4}E_{12}.$ |
| Input | $E_1 = 1, E_8 = 0.$ |

Similarly, in **Figure 4(b)** we divided the device configuration in **Figure 3(a)** into an add-drop MRR, two SIs, and several connecting waveguides between them. By using this new dividing method, we obtained the same response spectra as those in **Figures 3(b)** and **3(c)**. When plotting the response spectra, the forward and backward field transfer functions for the SIs were further expressed as

$$T_{SI-i} = \frac{E_2^+}{E_1^+} = \frac{E_6^+}{E_5^+} = (t_{SI-i}^2 - \kappa_{SI-i}^2)a_{SI-i}e^{j\varphi_{SI-i}}, \quad (i=1, 2) \quad (5)$$

$$R_{SI-i} = \frac{E_1^-}{E_1^+} = \frac{E_5^-}{E_5^+} = 2jt_{SI-i}\kappa_{SI-i}a_{SI-i}e^{j\varphi_{SI-i}}, \quad (i=1, 2) \quad (6)$$

where $j = \sqrt{-1}$, a_{SI-i} and φ_{SI-i} ($i = 1, 2$) are the round-trip transmission factor and phase shift along rings in the SIs, respectively. t_{SI-i} and κ_{SI-i} ($i = 1, 2$) are the self-coupling and cross coupling coefficients of the directional couplers in the SIs, respectively.

As shown in **Table 4**, only 10 equations are established by using the new dividing method, in contrast to 32 equations obtained for the dividing method in **Figure 3(a)**. This indicates that although dividing device into basic elements is a universal approach, dividing it into submodules simplifies the process of solving equations. This is particularly true for devices composed of multiple submodules, where the advantages of the new division method become even more evident.

Table 4. Scattering matrix equations for the device in **Figure 4(b)**. T_{SI-i} and R_{SI-i} ($i = 1, 2$) are forward and backward field transfer functions for the SIs, respectively. T_{RR} and D_{RR} are the field transfer functions at the through and drop ports for the AD-MRR, respectively.

| | | |
|------------------------------------|--|---|
| Scattering matrix equations | Sagnac interferometers (SIs) | $\begin{bmatrix} E_2^+ \\ E_1^+ \end{bmatrix} = \begin{bmatrix} T_{SI-1} & R_{SI-1} \\ R_{SI-1} & T_{SI-1} \end{bmatrix} \begin{bmatrix} E_1^+ \\ E_2^+ \end{bmatrix}, \begin{bmatrix} E_6^+ \\ E_5^+ \end{bmatrix} = \begin{bmatrix} T_{SI-2} & R_{SI-2} \\ R_{SI-2} & T_{SI-2} \end{bmatrix} \begin{bmatrix} E_5^+ \\ E_6^+ \end{bmatrix}.$ |
| | Add-drop micro-ring resonator (AD-MRR) | $\begin{bmatrix} E_4^+ \\ E_3^+ \end{bmatrix} = D_{RR} \begin{bmatrix} E_3^+ \\ E_4^+ \end{bmatrix}.$ |
| | Connecting waveguides | $\begin{bmatrix} E_3^+ \\ E_2^+ \end{bmatrix} = T_{w1} \begin{bmatrix} E_2^+ \\ E_3^+ \end{bmatrix}, \begin{bmatrix} E_5^+ \\ E_4^+ \end{bmatrix} = T_{w2} \begin{bmatrix} E_4^+ \\ E_5^+ \end{bmatrix}.$ |
| Input | $E_{1^+} = 1, E_{6^-} = 0.$ | |

In **Figure 5**, we model a more complex device by dividing it into eight SIs and establishing 32 linear equations, as summarized in **Table 5**. The forward and backward field transfer functions for the SIs are denoted as T_{SI-i} and R_{SI-i} ($i = 1 - 8$), respectively. Dividing the device into basic elements would result in a system of 64 equations, compared to the 32 equations shown in **Table 5**. By solving the system of 32 equations to obtain E_{16^+} and E_{1^-} , we obtain the spectral transfer functions at Port 2 and Port 1 (reflection), respectively. The corresponding response spectra are plotted in **Figures 5(b)** and **5(c)**, which are consistent with the results in Ref. [95] and further confirms the effectiveness of our method in modeling devices with complex configurations.

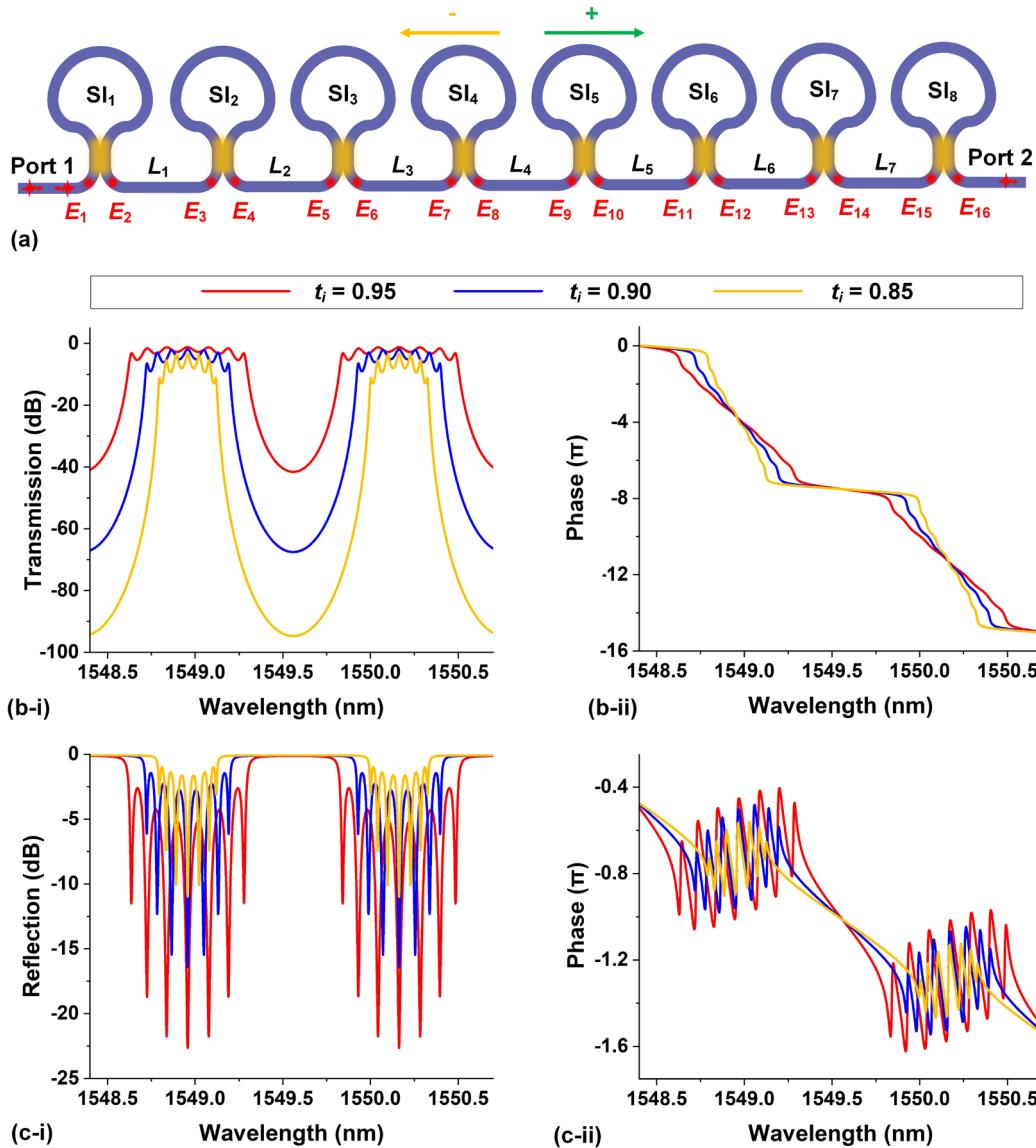


Figure 5. (a) Schematic illustration of an integrated photonic resonator formed by eight cascaded Sagnac interferometers (SIs) with input from Port 1. The device is divided into eight SIs and connecting waveguides between them, with E_i ($i = 1-16$) denoting the optical fields at the dividing points. The electric fields propagating from right to left are defined as “+” direction and the ones propagating from left to right are defined as “-” direction. (b) Calculated (i) power transmission and (ii) phase response spectra at Port 2 for different t_i ($i = 1-8$), which are the self-coupling coefficients of the directional couplers in SIs. (c) Calculated (i) power reflection and (ii) phase response spectra at Port 1 for different t_i ($i = 1-8$). In (b) and (c), the circumference of the rings in the SIs are $129.66 \mu\text{m}$, and the lengths of the connecting waveguides between them are $100 \mu\text{m}$.

Table 5. Scattering matrix equations for the device in Figure 5(a). T_{SI-i} and R_{SI-i} ($i = 1-8$) are the forward and backward field transfer functions for the SIs, respectively.

| | | |
|------------------------------------|------------------------------|--|
| Scattering matrix equations | Sagnac interferometers (SIs) | $\begin{bmatrix} E_2^+ \\ E_1^+ \end{bmatrix} = \begin{bmatrix} T_{SI-1} & R_{SI-1} \\ R_{SI-1} & T_{SI-1} \end{bmatrix} \begin{bmatrix} E_1^+ \\ E_2^+ \end{bmatrix}, \quad \begin{bmatrix} E_4^+ \\ E_3^+ \end{bmatrix} = \begin{bmatrix} T_{SI-2} & R_{SI-2} \\ R_{SI-2} & T_{SI-2} \end{bmatrix}$ |
| | | $\begin{bmatrix} E_6^+ \\ E_5^+ \end{bmatrix} = \begin{bmatrix} T_{SI-3} & R_{SI-3} \\ R_{SI-3} & T_{SI-3} \end{bmatrix} \begin{bmatrix} E_5^+ \\ E_6^+ \end{bmatrix}, \quad \begin{bmatrix} E_8^+ \\ E_7^+ \end{bmatrix} = \begin{bmatrix} T_{SI-4} & R_{SI-4} \\ R_{SI-4} & T_{SI-4} \end{bmatrix} \begin{bmatrix} E_7^+ \\ E_8^+ \end{bmatrix}$ |
| | | $\begin{bmatrix} E_{10}^+ \\ E_9^+ \end{bmatrix} = \begin{bmatrix} T_{SI-5} & R_{SI-5} \\ R_{SI-5} & T_{SI-5} \end{bmatrix} \begin{bmatrix} E_9^+ \\ E_{10}^+ \end{bmatrix}, \quad \begin{bmatrix} E_{12}^+ \\ E_{11}^+ \end{bmatrix} = \begin{bmatrix} T_{SI-6} & R_{SI-6} \\ R_{SI-6} & T_{SI-6} \end{bmatrix} \begin{bmatrix} E_{11}^+ \\ E_{12}^+ \end{bmatrix}$ |
| | | $\begin{bmatrix} E_{14}^+ \\ E_{13}^+ \end{bmatrix} = \begin{bmatrix} T_{SI-7} & R_{SI-7} \\ R_{SI-7} & T_{SI-7} \end{bmatrix} \begin{bmatrix} E_{13}^+ \\ E_{14}^+ \end{bmatrix}, \quad \begin{bmatrix} E_{16}^+ \\ E_{15}^+ \end{bmatrix} = \begin{bmatrix} T_{SI-8} & R_{SI-8} \\ R_{SI-8} & T_{SI-8} \end{bmatrix} \begin{bmatrix} E_{15}^+ \\ E_{16}^+ \end{bmatrix}$ |

| | |
|--------------------------|---|
| Connecting waveguides | $\begin{bmatrix} E_3^+ \\ E_2^- \end{bmatrix} = T_{w1} \begin{bmatrix} E_2^+ \\ E_3^- \end{bmatrix}, \begin{bmatrix} E_5^+ \\ E_4^- \end{bmatrix} = T_{w2} \begin{bmatrix} E_4^+ \\ E_5^- \end{bmatrix}, \begin{bmatrix} E_7^+ \\ E_6^- \end{bmatrix} = T_{w3} \begin{bmatrix} E_6^+ \\ E_7^- \end{bmatrix},$ $\begin{bmatrix} E_9^+ \\ E_8^- \end{bmatrix} = T_{w4} \begin{bmatrix} E_8^+ \\ E_9^- \end{bmatrix}, \begin{bmatrix} E_{11}^+ \\ E_{10}^- \end{bmatrix} = T_{w5} \begin{bmatrix} E_{10}^+ \\ E_{11}^- \end{bmatrix}, \begin{bmatrix} E_{13}^+ \\ E_{12}^- \end{bmatrix} = T_{w6} \begin{bmatrix} E_{12}^+ \\ E_{13}^- \end{bmatrix},$ $\begin{bmatrix} E_{15}^+ \\ E_{14}^- \end{bmatrix} = T_{w7} \begin{bmatrix} E_{14}^+ \\ E_{15}^- \end{bmatrix}.$ |
| Input | $E_{16}^+ = 1, E_{16}^- = 0.$ |

When dividing complex devices into submodules, it's important to ensure that the submodules are independent. Here, "independent" means that the submodules exchange energy with other parts exclusively through connecting waveguides. For the device shown in **Figure 6a** formed by a self-coupled waveguide, even though there are multiple SIs within the device, it cannot be divided into submodules of SIs. This is because the adjacent SIs are mutually coupled with energy exchange through directional couplers. In this case, the spectral transfer functions can be obtained by using the universal dividing method, which divides the device into basic elements of directional couplers and connecting waveguides.

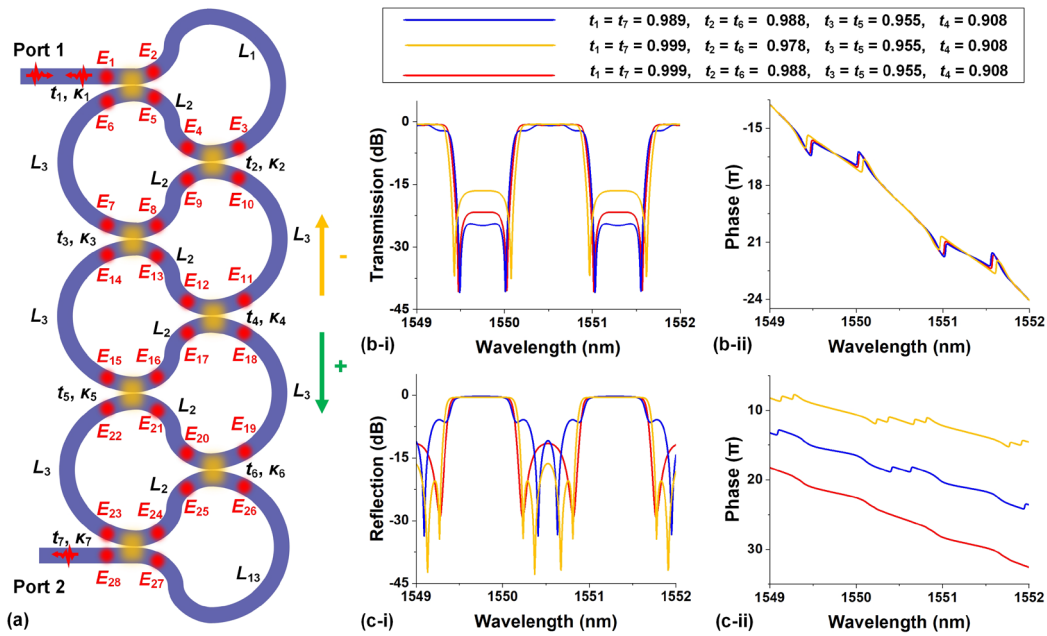


Figure 6. (a) Schematic illustration of an integrated photonic resonator formed by a self-coupled waveguide with input from Port 1. The device is divided into several directional couplers and connecting waveguides, with E_i ($i = 1-28$) denoting the optical fields at the dividing points. The electric fields propagating from top to down are defined as "+" direction and the ones propagating from down to top are defined as "-" direction. (b) Calculated (i) power transmission and (ii) phase response spectra at Port 2 for different t_i , which are the self-coupling coefficients of the directional couplers. (c) Calculated (i) power reflection and (ii) phase response spectra at Port 1 for different t_i .

Table 6 shows a system of 56 equations obtained by using the universal dividing method for the device in **Figure 6a**. By solving these equations to obtain E_{28}^+ and E_{16}^- , we obtain the spectral transfer functions at Port 1 and Port 2, respectively. The corresponding response spectra for different t_i are shown in **Figures 6(b)** and **6(c)**. Except for t_i , all other structural parameters are kept constant as: $L_1 = 180 \mu\text{m}$, $L_2 = 60 \mu\text{m}$ and $L_3 = 120 \mu\text{m}$. The response spectra also show a good agreement with the results in Ref. [24], providing additional evidence of the effectiveness of our method.

Table 6. Definitions of structural parameters of the device in Figure 6(a) and the corresponding scattering matrix equations.

| Directional | Structural | Field transmission coefficient | Field cross coupling coefficient |
|-------------|------------|--------------------------------|----------------------------------|
|-------------|------------|--------------------------------|----------------------------------|

| couplers | | Parameters ($i = 1 - 7$) | t_i | κ_i | | | |
|---|--|-------------------------------|--|--|---|---|--|
| Scattering matrix equations | | | $\begin{bmatrix} E_2^+ \\ E_5^- \end{bmatrix} = \begin{bmatrix} t_1 & j\kappa_1 \\ j\kappa_1 & t_1 \end{bmatrix} \begin{bmatrix} E_1^+ \\ E_6^- \end{bmatrix}$ | $\begin{bmatrix} E_1^- \\ E_6^+ \end{bmatrix} = \begin{bmatrix} t_1 & j\kappa_1 \\ j\kappa_1 & t_1 \end{bmatrix} \begin{bmatrix} E_2^- \\ E_5^+ \end{bmatrix}$ | | | |
| | | | $\begin{bmatrix} E_4^+ \\ E_9^- \end{bmatrix} = \begin{bmatrix} t_2 & j\kappa_2 \\ j\kappa_2 & t_2 \end{bmatrix} \begin{bmatrix} E_3^+ \\ E_{10}^- \end{bmatrix}$ | $\begin{bmatrix} E_3^- \\ E_{10}^+ \end{bmatrix} = \begin{bmatrix} t_2 & j\kappa_2 \\ j\kappa_2 & t_2 \end{bmatrix} \begin{bmatrix} E_4^- \\ E_9^+ \end{bmatrix}$ | | | |
| | | | $\begin{bmatrix} E_8^+ \\ E_{13}^- \end{bmatrix} = \begin{bmatrix} t_3 & j\kappa_3 \\ j\kappa_3 & t_3 \end{bmatrix} \begin{bmatrix} E_7^+ \\ E_{14}^- \end{bmatrix}$ | $\begin{bmatrix} E_7^- \\ E_{14}^+ \end{bmatrix} = \begin{bmatrix} t_3 & j\kappa_3 \\ j\kappa_3 & t_3 \end{bmatrix} \begin{bmatrix} E_8^- \\ E_{13}^+ \end{bmatrix}$ | | | |
| | | | $\begin{bmatrix} E_{12}^+ \\ E_{17}^- \end{bmatrix} = \begin{bmatrix} t_4 & j\kappa_4 \\ j\kappa_4 & t_4 \end{bmatrix} \begin{bmatrix} E_{11}^+ \\ E_{18}^- \end{bmatrix}$ | $\begin{bmatrix} E_{18}^- \\ E_{11}^+ \end{bmatrix} = \begin{bmatrix} t_4 & j\kappa_4 \\ j\kappa_4 & t_4 \end{bmatrix} \begin{bmatrix} E_{12}^- \\ E_{17}^+ \end{bmatrix}$ | | | |
| | | | $\begin{bmatrix} E_{16}^+ \\ E_{21}^- \end{bmatrix} = \begin{bmatrix} t_5 & j\kappa_5 \\ j\kappa_5 & t_5 \end{bmatrix} \begin{bmatrix} E_{15}^+ \\ E_{22}^- \end{bmatrix}$ | $\begin{bmatrix} E_{15}^- \\ E_{22}^+ \end{bmatrix} = \begin{bmatrix} t_5 & j\kappa_5 \\ j\kappa_5 & t_5 \end{bmatrix} \begin{bmatrix} E_{16}^- \\ E_{21}^+ \end{bmatrix}$ | | | |
| | | | $\begin{bmatrix} E_{20}^+ \\ E_{25}^- \end{bmatrix} = \begin{bmatrix} t_6 & j\kappa_6 \\ j\kappa_6 & t_6 \end{bmatrix} \begin{bmatrix} E_{19}^+ \\ E_{26}^- \end{bmatrix}$ | $\begin{bmatrix} E_{19}^- \\ E_{26}^+ \end{bmatrix} = \begin{bmatrix} t_6 & j\kappa_6 \\ j\kappa_6 & t_6 \end{bmatrix} \begin{bmatrix} E_{20}^- \\ E_{25}^+ \end{bmatrix}$ | | | |
| | | | $\begin{bmatrix} E_{24}^+ \\ E_{27}^- \end{bmatrix} = \begin{bmatrix} t_7 & j\kappa_7 \\ j\kappa_7 & t_7 \end{bmatrix} \begin{bmatrix} E_{23}^+ \\ E_{28}^- \end{bmatrix}$ | $\begin{bmatrix} E_{23}^- \\ E_{28}^+ \end{bmatrix} = \begin{bmatrix} t_7 & j\kappa_7 \\ j\kappa_7 & t_7 \end{bmatrix} \begin{bmatrix} E_{24}^- \\ E_{27}^+ \end{bmatrix}$ | | | |
| Structural Parameters ($i = 1 - 3$) | | Length | Transmission factor | Phase shift | | | |
| | | L_i | a_i | φ_i | | | |
| Connecting waveguides Scattering matrix equations | | | $\begin{bmatrix} E_3^+ \\ E_2^- \end{bmatrix} = T_1 \begin{bmatrix} E_2^+ \\ E_3^- \end{bmatrix}$ | $\begin{bmatrix} E_5^+ \\ E_4^- \end{bmatrix} = T_2 \begin{bmatrix} E_4^+ \\ E_5^- \end{bmatrix}$ | $\begin{bmatrix} E_7^+ \\ E_6^- \end{bmatrix} = T_3 \begin{bmatrix} E_6^+ \\ E_7^- \end{bmatrix}$ | $\begin{bmatrix} E_9^+ \\ E_8^- \end{bmatrix} = T_2 \begin{bmatrix} E_8^+ \\ E_9^- \end{bmatrix}$ | |
| | | | $\begin{bmatrix} E_{11}^+ \\ E_{10}^- \end{bmatrix} = T_3 \begin{bmatrix} E_{10}^+ \\ E_{11}^- \end{bmatrix}$ | $\begin{bmatrix} E_{13}^+ \\ E_{12}^- \end{bmatrix} = T_2 \begin{bmatrix} E_{12}^+ \\ E_{13}^- \end{bmatrix}$ | $\begin{bmatrix} E_{15}^+ \\ E_{14}^- \end{bmatrix} = T_3 \begin{bmatrix} E_{14}^+ \\ E_{15}^- \end{bmatrix}$ | $\begin{bmatrix} E_{17}^+ \\ E_{16}^- \end{bmatrix} = T_2 \begin{bmatrix} E_{16}^+ \\ E_{17}^- \end{bmatrix}$ | |
| | | | | $\begin{bmatrix} E_{19}^+ \\ E_{18}^- \end{bmatrix} = T_3 \begin{bmatrix} E_{18}^+ \\ E_{19}^- \end{bmatrix}$ | $\begin{bmatrix} E_{21}^+ \\ E_{20}^- \end{bmatrix} = T_2 \begin{bmatrix} E_{20}^+ \\ E_{21}^- \end{bmatrix}$ | | |
| | | | $\begin{bmatrix} E_{23}^+ \\ E_{22}^- \end{bmatrix} = T_3 \begin{bmatrix} E_{22}^+ \\ E_{23}^- \end{bmatrix}$ | $\begin{bmatrix} E_{25}^+ \\ E_{24}^- \end{bmatrix} = T_2 \begin{bmatrix} E_{24}^+ \\ E_{25}^- \end{bmatrix}$ | $\begin{bmatrix} E_{27}^+ \\ E_{26}^- \end{bmatrix} = T_1 \begin{bmatrix} E_{26}^+ \\ E_{27}^- \end{bmatrix}$ | | |
| Input | | $E_{1^+} = 1, E_{28^-} = 0.$ | | | | | |

5. Deviations Induced by Approximations

As evidenced by the results in previous sections, our method proves effective for modeling integrated photonic resonators and shows advantages for modeling those with complex configurations. Despite this, the method still has limitations that could cause deviations between the simulation results and measurements for practical devices. In this section, we discuss the limitations of our method to model integrated photonic resonators and methods for improving modeling accuracy.

In our modeling, we assume the self-coupling coefficient t and cross-coupling coefficient κ of the directional couplers to be wavelength-independent constant, while this holds true only within a certain wavelength range. According to Ref. [34, 95, 32], the field cross-coupling coefficient κ of a directional coupler with a coupling length of L_c can be given by

$$\kappa = \sin\left(\frac{\pi}{2} \cdot \frac{L_c}{L_x}\right), \quad (7)$$

where L_x is the cross-over length, defined as the minimum distance at which optical power completely transfers from one waveguide to the other. The L_x can be further expressed as [95]

$$L_x = \frac{\lambda}{2(n_{eff, even} - n_{eff, odd})}. \quad (8)$$

where λ is the light wavelength, $n_{eff, even}$ and $n_{eff, odd}$ are the effective indices of the two fundamental eigenmodes of the coupled waveguides, respectively. From Eqs. (7) and (8), it can be seen that the coupling strength of the directional coupler is actually wavelength dependent due to the existence of dispersion (which leads to wavelength-dependent values of $n_{eff, even}$ and $n_{eff, odd}$). Therefore, the variation in the coupling strength of the directional couplers with wavelength can no longer be ignored when modeling the device's response spectra over a broad bandwidth (typically > 30 nm).

Another potential limitation arises from the fact that we use a constant waveguide group index n_g instead of wavelength-dependent waveguide effective index n_{eff} when calculating the phase shift along waveguides. In fact, the relation between n_g and n_{eff} can be expressed as [94]:

$$n_g = n_{eff}(\lambda) - \lambda \frac{dn_{eff}(\lambda)}{d\lambda}, \quad (9)$$

where $n_{eff}(\lambda)$ is the effective index as a function of light wavelength λ . The group index n_g is widely used for calculating the free spectral ranges (FSRs) of integrated photonic resonators. For example, the FSR for a MRR can be approximately given by [94]

$$\lambda_{FSR} \approx \frac{\lambda_0^2}{n_g L}, \quad (10)$$

where λ_0 is the resonance wavelength and L is the ring circumference.

Similar to the cross-coupling coefficient κ of a directional coupler, the group index n_g can be regarded as a constant coefficient only within a specific wavelength range. In contrast to introducing n_{eff} at different wavelengths, using a constant n_g can greatly simplify the plotting of the response spectra based on the spectral transfer function. However, this approximation only holds for modeling spectral response over a relatively narrow wavelength range (e.g., < 30 nm). When modeling the spectral response over a broad bandwidth or for nonlinear optical devices that are sensitive to dispersion-induced phase mismatch [8,96–128], the wavelength-dependent n_{eff} should be used to achieve more accurate simulation results.

6. Conclusion

In summary, a universal approach for modeling integrated photonic resonators with complex structures is proposed based on the SMM. By dividing the device configuration into basic elements such as directional couplers and connecting waveguides, our approach shows effectiveness in modeling integrated photonic resonators with both unidirectional and bidirectional light propagation, with the simulated spectral response agreeing well with experimental results. By dividing the device configuration into independent submodules MRRs and SIs, the modeling in our approach can also be simplified. Finally, we discuss the limitations arising from approximations in our modeling and the corresponding strategies for improving modeling accuracy. Our approach offers an efficient way for designing and optimizing complex integrated photonic devices, which is applicable across a wide range of integrated platforms.

Conflicts of Interest: The authors declare no conflicts of interest.

References

1. Q. Xu, B. Schmidt, S. Pradhan, and M. Lipson, "Micrometre-scale silicon electro-optic modulator," *Nature*, vol. 435, no. 7040, pp. 325-327, 2005/05/01, 2005.
2. P. Marin-Palomo, J. N. Kemal, M. Karpov, A. Kordts, J. Pfeifle, M. H. P. Pfeiffer, P. Trocha, S. Wolf, V. Brasch, M. H. Anderson, R. Rosenberger, K. Vijayan, W. Freude, T. J. Kippenberg, and C. Koos, "Microresonator-based solitons for massively parallel coherent optical communications," *Nature*, vol. 546, no. 7657, pp. 274-279, 2017/06/01, 2017.
3. S. Schuler, J. E. Muench, A. Ruocco, O. Balci, D. v. Thourhout, V. Sorianello, M. Romagnoli, K. Watanabe, T. Taniguchi, I. Goykhman, A. C. Ferrari, and T. Mueller, "High-responsivity graphene photodetectors integrated on silicon microring resonators," *Nature Communications*, vol. 12, no. 1, pp. 3733, 2021/06/18, 2021.
4. W. Liu, M. Li, R. S. Guzzon, E. J. Norberg, J. S. Parker, M. Lu, L. A. Coldren, and J. Yao, "A fully reconfigurable photonic integrated signal processor," *Nature Photonics*, vol. 10, no. 3, pp. 190-195, 2016/03/01, 2016.
5. J. Wu, P. Cao, X. Hu, X. Jiang, T. Pan, Y. Yang, C. Qiu, C. Tremblay, and Y. Su, "Compact tunable silicon photonic differential-equation solver for general linear time-invariant systems," *Optics Express*, vol. 22, no. 21, pp. 26254-26264, 2014/10/20, 2014.
6. J. Wu, B. Liu, J. Peng, J. Mao, X. Jiang, C. Qiu, C. Tremblay, and Y. Su, "On-chip tunable second-order differential-equation solver based on a silicon photonic mode-split microresonator," *Journal of Lightwave Technology*, vol. 33, no. 17, pp. 3542-3549, 2015/09/01, 2015.

7. T. J. Kippenberg, R. Holzwarth, and S. A. Diddams, "Microresonator-based optical frequency combs," *Science*, vol. 332, no. 6029, pp. 555-559, 2011/04/29, 2011.
8. J. Wu, Y. Yang, Y. Qu, L. Jia, Y. Zhang, X. Xu, S. T. Chu, B. E. Little, R. Morandotti, B. Jia, and D. J. Moss, "2D layered graphene oxide films integrated with micro-ring resonators for enhanced nonlinear optics," *Small*, vol. 16, no. 16, pp. 1906563, 2020.
9. A. Guarino, G. Poberaj, D. Rezzonico, R. Degl'Innocenti, and P. Günter, "Electro-optically tunable microring resonators in lithium niobate," *Nature Photonics*, vol. 1, no. 7, pp. 407-410, 2007/07/01, 2007.
10. S. N. Zheng, J. Zou, H. Cai, J. F. Song, L. K. Chin, P. Y. Liu, Z. P. Lin, D. L. Kwong, and A. Q. Liu, "Microring resonator-assisted Fourier transform spectrometer with enhanced resolution and large bandwidth in single chip solution," *Nature Communications*, vol. 10, no. 1, pp. 2349, 2019/05/28, 2019.
11. C. Chung-Yen, W. Fung, and L. J. Guo, "Polymer microring resonators for biochemical sensing applications," *IEEE Journal of Selected Topics in Quantum Electronics*, vol. 12, no. 1, pp. 134-142, 2006.
12. P. P. Khial, A. D. White, and A. Hajimiri, "Nanophotonic optical gyroscope with reciprocal sensitivity enhancement," *Nature Photonics*, vol. 12, no. 11, pp. 671-675, 2018/11/01, 2018.
13. B. Dong, F. Brücknerhoff-Plückelmann, L. Meyer, J. Dijkstra, I. Bente, D. Wendland, A. Varri, S. Aggarwal, N. Farmakidis, M. Wang, G. Yang, J. S. Lee, Y. He, E. Gooskens, D.-L. Kwong, P. Bienstman, W. H. P. Pernice, and H. Bhaskaran, "Partial coherence enhances parallelized photonic computing," *Nature*, vol. 632, no. 8023, pp. 55-62, 2024/08/01, 2024.
14. N. Farmakidis, B. Dong, and H. Bhaskaran, "Integrated photonic neuromorphic computing: opportunities and challenges," *Nature Reviews Electrical Engineering*, vol. 1, no. 6, pp. 358-373, 2024/06/01, 2024.
15. S. Biasi, G. Donati, A. Lugnan, M. Mancinelli, E. Staffoli, and L. Pavesi, "Photonic neural networks based on integrated silicon microresonators," *Intelligent Computing*, vol. 3, pp. 0067.
16. A. Yariv, "Universal relations for coupling of optical power between microresonators and dielectric waveguides," *Electronics Letters*, 36, 2000].
17. L. Zhou, T. Ye, and J. Chen, "Coherent interference induced transparency in self-coupled optical waveguide-based resonators," *Optics Letters*, vol. 36, no. 1, pp. 13-15, 2011/01/01, 2011.
18. M. C. M. M. Souza, L. A. M. Barea, F. Vallini, G. F. M. Rezende, G. S. Wiederhecker, and N. C. Frateschi, "Embedded coupled microrings with high-finesse and close-spaced resonances for optical signal processing," *Optics Express*, vol. 22, no. 9, pp. 10430-10438, 2014/05/05, 2014.
19. H. Arianfard, J. Wu, S. Juodkazis, and D. J. Moss, "Three waveguide coupled Sagnac loop reflectors for advanced spectral engineering," *Journal of Lightwave Technology*, vol. 39, no. 11, pp. 3478-3487, 2021/06/01, 2021.
20. H. Arianfard, J. Wu, S. Juodkazis, and D. J. Moss, "Advanced multi-functional integrated photonic filters based on coupled Sagnac loop reflectors," *Journal of Lightwave Technology*, vol. 39, no. 5, pp. 1400-1408, 2021.
21. H. Arianfard, J. Wu, S. Juodkazis, and D. J. Moss, "Spectral shaping based on coupled Sagnac loop reflectors formed by a self-coupled wire waveguide," *IEEE Photonics Technology Letters*, vol. 33, no. 13, pp. 680-683, 2021.
22. H. Arianfard, J. Wu, S. Juodkazis, and D. J. Moss, "Optical analogs of rabi splitting in integrated waveguide-coupled resonators," *Advanced Physics Research*, vol. 2, no. 9, pp. 2200123, 2023/09/01, 2023.
23. H. Arianfard, S. Juodkazis, D. J. Moss, and J. Wu, "Sagnac interference in integrated photonics," *Applied Physics Reviews*, vol. 10, no. 1, pp. 011309, 2023/03/01, 2023.
24. S. Lai, Z. Xu, B. Liu, and J. Wu, "Compact silicon photonic interleaver based on a self-coupled optical waveguide," *Applied Optics*, vol. 55, no. 27, pp. 7550-7555, 2016/09/20, 2016.
25. J. Wu, T. Moein, X. Xu, G. Ren, A. Mitchell, and D. J. Moss, "Micro-ring resonator quality factor enhancement via an integrated Fabry-Perot cavity," *APL Photonics*, vol. 2, no. 5, pp. 056103, 2017.
26. C. Qiu, P. Yu, T. Hu, F. Wang, X. Jiang, and J. Yang, "Asymmetric Fano resonance in eye-like microring system," *Applied Physics Letters*, vol. 101, no. 2, 2012.
27. D. J. Moss, R. Morandotti, A. L. Gaeta, and M. Lipson, "New CMOS-compatible platforms based on silicon nitride and Hydex for nonlinear optics," *Nature Photonics*, vol. 7, no. 8, pp. 597-607, 2013/08/01, 2013.
28. G. Poberaj, H. Hu, W. Sohler, and P. Günter, "Lithium niobate on insulator (LNOI) for micro-photonics devices," *Laser & Photonics Reviews*, vol. 6, no. 4, pp. 488-503, 2012/07/16, 2012.
29. M. Ferrera, L. Razzari, D. Duchesne, R. Morandotti, Z. Yang, M. Liscidini, J. E. Sipe, S. Chu, B. E. Little, and D. J. Moss, "Low-power continuous-wave nonlinear optics in doped silica glass integrated waveguide structures," *Nature Photonics*, vol. 2, no. 12, pp. 737-740, 2008/12/01, 2008.
30. Y. Qu, J. Wu, Y. Yang, Y. Zhang, Y. Liang, H. El Dirani, R. Crochemore, P. Demongodin, C. Sciancalepore, C. Grillet, C. Monat, B. Jia, and D. J. Moss, "Enhanced four-wave mixing in silicon nitride waveguides integrated with 2D layered graphene oxide films," *Advanced Optical Materials*, vol. 8, no. 23, pp. 2001048, 2020/12/01, 2020.
31. L. Razzari, et al., "CMOS-compatible integrated optical hyper-parametric oscillator," *Nature Photonics*, vol. 4, no. 1, pp. 41-45, 2010.

32. A. Pasquazi, et al., "Sub-picosecond phase-sensitive optical pulse characterization on a chip", *Nature Photonics*, vol. 5, no. 10, pp. 618-623 (2011).
33. M Ferrera et al., "On-Chip ultra-fast 1st and 2nd order CMOS compatible all-optical integration", *Optics Express* vol. 19 (23), 23153-23161 (2011).
34. Bao, C., et al., Direct soliton generation in microresonators, *Opt. Lett.*, 42, 2519 (2017).
35. M.Ferrera et al., "CMOS compatible integrated all-optical RF spectrum analyzer", *Optics Express*, vol. 22, no. 18, 21488 - 21498 (2014).
36. M. Kues, et al., "Passively modelocked laser with an ultra-narrow spectral width", *Nature Photonics*, vol. 11, no. 3, pp. 159, 2017.
37. M.Ferrera et al."On-Chip ultra-fast 1st and 2nd order CMOS compatible all-optical integration", *Opt. Express*, vol. 19, (23)pp. 23153-23161 (2011).
38. D. Duchesne, M. Peccianti, M. R. E. Lamont, et al., "Supercontinuum generation in a high index doped silica glass spiral waveguide," *Optics Express*, vol. 18, no. 2, pp. 923-930, 2010.
39. H Bao, L Olivieri, M Rowley, ST Chu, BE Little, R Morandotti, DJ Moss, ... "Turing patterns in a fiber laser with a nested microresonator: Robust and controllable microcomb generation", *Physical Review Research* vol. 2 (2), 023395 (2020).
40. M. Ferrera, et al., "On-chip CMOS-compatible all-optical integrator", *Nature Communications*, vol. 1, Article 29, 2010.
41. A. Pasquazi, et al., "All-optical wavelength conversion in an integrated ring resonator," *Optics Express*, vol. 18, no. 4, pp. 3858-3863, 2010.
42. A.Pasquazi, Y. Park, J. Azana, et al., "Efficient wavelength conversion and net parametric gain via Four Wave Mixing in a high index doped silica waveguide," *Optics Express*, vol. 18, no. 8, pp. 7634-7641, 2010.
43. Peccianti, M. Ferrera, L. Razzari, et al., "Subpicosecond optical pulse compression via an integrated nonlinear chirper," *Optics Express*, vol. 18, no. 8, pp. 7625-7633, 2010.
44. M Ferrera, Y Park, L Razzari, BE Little, ST Chu, R Morandotti, DJ Moss, ... et al., "All-optical 1st and 2nd order integration on a chip", *Optics Express* vol. 19 (23), 23153-23161 (2011).
45. M. Ferrera et al., "Low Power CW Parametric Mixing in a Low Dispersion High Index Doped Silica Glass Micro-Ring Resonator with Q-factor > 1 Million", *Optics Express*, vol.17, no. 16, pp. 14098-14103 (2009).
46. M. Peccianti, et al., "Demonstration of an ultrafast nonlinear microcavity modelocked laser", *Nature Communications*, vol. 3, pp. 765, 2012.
47. A.Pasquazi, et al., "Self-locked optical parametric oscillation in a CMOS compatible microring resonator: a route to robust optical frequency comb generation on a chip," *Optics Express*, vol. 21, no. 11, pp. 13333-13341, 2013.
48. A.Pasquazi, et al., "Stable, dual mode, high repetition rate mode-locked laser based on a microring resonator," *Optics Express*, vol. 20, no. 24, pp. 27355-27362, 2012.
49. Pasquazi, A. et al. Micro-combs: a novel generation of optical sources. *Physics Reports* 729, 1-81 (2018).
50. Yang Sun, Jiayang Wu, Mengxi Tan, Xingyuan Xu, Yang Li, Roberto Morandotti, Arnan Mitchell, and David J. Moss, "Applications of optical micro-combs", *Advances in Optics and Photonics* **15** (1) 86-175 (2023). <https://doi.org/10.1364/AOP.470264>.
51. H. Bao, et al., Laser cavity-soliton microcombs, *Nature Photonics*, vol. 13, no. 6, pp. 384-389, Jun. 2019.
52. Antonio Cutrona, Maxwell Rowley, Debayan Das, Luana Olivieri, Luke Peters, Sai T. Chu, Brent L. Little, Roberto Morandotti, David J. Moss, Juan Sebastian Toterogongora, Marco Peccianti, Alessia Pasquazi, "High Conversion Efficiency in Laser Cavity-Soliton Microcombs", *Optics Express* Vol. 30, Issue 22, pp. 39816-39825 (2022). <https://doi.org/10.1364/OE.470376>.
53. M.Rowley, P.Hanzard, A.Cutrona, H.Bao, S.Chu, B.Little, R.Morandotti, D. J. Moss, G. Oppo, J. Gongora, M. Peccianti and A. Pasquazi, "Self-emergence of robust solitons in a micro-cavity", *Nature* vol. 608 (7922) 303-309 (2022).
54. A. Cutrona, M. Rowley, A. Bendahmane, V. Cecconi, L. Peters, L. Olivieri, B. E. Little, S. T. Chu, S. Stivala, R. Morandotti, D. J. Moss, J. S. Toterogongora, M. Peccianti, A. Pasquazi, "Nonlocal bonding of a soliton and a blue-detuned state in a microcomb laser", *Nature Communications Physics* **6** Article 259 (2023). <https://doi.org/10.1038/s42005-023-01372-0>.
55. Aadhi A. Rahim, Imtiaz Alamgir, Luigi Di Lauro, Bennet Fischer, Nicolas Perron, Pavel Dmitriev, Celine Mazoukh, Piotr Roztocki, Cristina Rimoldi, Mario Chemnitz, Armaghan Eshaghi, Evgeny A. Viktorov, Anton V. Kovalev, Brent E. Little, Sai T. Chu, David J. Moss, and Roberto Morandotti, "Mode-locked laser with multiple timescales in a microresonator-based nested cavity", *APL Photonics* **9** 031302 (2024). DOI:10.1063/5.0174697.
56. A. Cutrona, M. Rowley, A. Bendahmane, V. Cecconi, L. Peters, L. Olivieri, B. E. Little, S. T. Chu, S. Stivala, R. Morandotti, D. J. Moss, J. S. Toterogongora, M. Peccianti, A. Pasquazi, "Stability Properties of Laser Cavity-Solitons for Metrological Applications", *Applied Physics Letters* vol. 122 (12) 121104 (2023); doi: 10.1063/5.0134147.

57. X. Xu, J. Wu, M. Shoeiby, T. G. Nguyen, S. T. Chu, B. E. Little, R. Morandotti, A. Mitchell, and D. J. Moss, "Reconfigurable broadband microwave photonic intensity differentiator based on an integrated optical frequency comb source," *APL Photonics*, vol. 2, no. 9, 096104, Sep. 2017.
58. Xu, X., et al., Photonic microwave true time delays for phased array antennas using a 49 GHz FSR integrated micro-comb source, *Photonics Research*, vol. 6, B30-B36 (2018).
59. X. Xu, M. Tan, J. Wu, R. Morandotti, A. Mitchell, and D. J. Moss, "Microcomb-based photonic RF signal processing", *IEEE Photonics Technology Letters*, vol. 31 no. 23 1854-1857, 2019.
60. Xu, et al., "Advanced adaptive photonic RF filters with 80 taps based on an integrated optical micro-comb source," *Journal of Lightwave Technology*, vol. 37, no. 4, pp. 1288-1295 (2019).
61. X. Xu, et al., "Photonic RF and microwave integrator with soliton crystal microcombs", *IEEE Transactions on Circuits and Systems II: Express Briefs*, vol. 67, no. 12, pp. 3582-3586, 2020. DOI:10.1109/TCSII.2020.2995682.
62. X. Xu, et al., "High performance RF filters via bandwidth scaling with Kerr micro-combs," *APL Photonics*, vol. 4 (2) 026102. 2019.
63. M. Tan, et al., "Microwave and RF photonic fractional Hilbert transformer based on a 50 GHz Kerr micro-comb", *Journal of Lightwave Technology*, vol. 37, no. 24, pp. 6097 – 6104, 2019.
64. M. Tan, et al., "RF and microwave fractional differentiator based on photonics", *IEEE Transactions on Circuits and Systems: Express Briefs*, vol. 67, no.11, pp. 2767-2771, 2020. DOI:10.1109/TCSII.2020.2965158.
65. M. Tan, et al., "Photonic RF arbitrary waveform generator based on a soliton crystal micro-comb source", *Journal of Lightwave Technology*, vol. 38, no. 22, pp. 6221-6226 (2020). DOI: 10.1109/JLT.2020.3009655.
66. M. Tan, X. Xu, J. Wu, R. Morandotti, A. Mitchell, and D. J. Moss, "RF and microwave high bandwidth signal processing based on Kerr Micro-combs", *Advances in Physics X*, VOL. 6, NO. 1, 1838946 (2021). DOI:10.1080/23746149.2020.1838946.
67. 123. X. Xu, et al., "Advanced RF and microwave functions based on an integrated optical frequency comb source," *Opt. Express*, vol. 26 (3) 2569 (2018).
68. M. Tan, X. Xu, J. Wu, B. Corcoran, A. Boes, T. G. Nguyen, S. T. Chu, B. E. Little, R. Morandotti, A. Lowery, A. Mitchell, and D. J. Moss, "Highly Versatile Broadband RF Photonic Fractional Hilbert Transformer Based on a Kerr Soliton Crystal Microcomb", *Journal of Lightwave Technology* vol. 39 (24) 7581-7587 (2021).
69. Wu, J. et al. RF Photonics: An Optical Microcombs' Perspective. *IEEE Journal of Selected Topics in Quantum Electronics* Vol. 24, 6101020, 1-20 (2018).
70. T. G. Nguyen et al., "Integrated frequency comb source-based Hilbert transformer for wideband microwave photonic phase analysis," *Opt. Express*, vol. 23, no. 17, pp. 22087-22097, Aug. 2015.
71. X. Xu, et al., "Broadband RF channelizer based on an integrated optical frequency Kerr comb source," *Journal of Lightwave Technology*, vol. 36, no. 19, pp. 4519-4526, 2018.
72. X. Xu, et al., "Continuously tunable orthogonally polarized RF optical single sideband generator based on micro-ring resonators," *Journal of Optics*, vol. 20, no. 11, 115701. 2018.
73. X. Xu, et al., "Orthogonally polarized RF optical single sideband generation and dual-channel equalization based on an integrated microring resonator," *Journal of Lightwave Technology*, vol. 36, no. 20, pp. 4808-4818. 2018.
74. X. Xu, et al., "Photonic RF phase-encoded signal generation with a microcomb source", *J. Lightwave Technology*, vol. 38, no. 7, 1722-1727, 2020.
75. X. Xu, et al., Broadband microwave frequency conversion based on an integrated optical micro-comb source", *Journal of Lightwave Technology*, vol. 38 no. 2, pp. 332-338, 2020.
76. M. Tan, et al., "Photonic RF and microwave filters based on 49GHz and 200GHz Kerr microcombs", *Optics Comm.* vol. 465,125563, Feb. 22. 2020.
77. X. Xu, et al., "Broadband photonic RF channelizer with 90 channels based on a soliton crystal microcomb", *Journal of Lightwave Technology*, Vol. 38, no. 18, pp. 5116 – 5121 (2020). doi: 10.1109/JLT.2020.2997699.
78. M. Tan et al., "Orthogonally polarized Photonic Radio Frequency single sideband generation with integrated micro-ring resonators", *IOP Journal of Semiconductors*, Vol. 42 (4), 041305 (2021). DOI: 10.1088/1674-4926/42/4/041305.
79. Mengxi Tan, X. Xu, J. Wu, T. G. Nguyen, S. T. Chu, B. E. Little, R. Morandotti, A. Mitchell, and David J. Moss, "Photonic Radio Frequency Channelizers based on Kerr Optical Micro-combs", *IOP Journal of Semiconductors* Vol. 42 (4), 041302 (2021). DOI:10.1088/1674-4926/42/4/041302.
80. B. Corcoran, et al., "Ultra-dense optical data transmission over standard fiber with a single chip source", *Nature Communications*, vol. 11, Article:2568, 2020.
81. X. Xu et al., "Photonic perceptron based on a Kerr microcomb for scalable high speed optical neural networks", *Laser and Photonics Reviews*, vol. 14, no. 8, 2000070 (2020). DOI: 10.1002/lpor.202000070.
82. X. Xu, et al., "11 TOPs photonic convolutional accelerator for optical neural networks", *Nature* vol. 589, 44-51 (2021).
83. Xingyuan Xu, Weiwei Han, Mengxi Tan, Yang Sun, Yang Li, Jiayang Wu, Roberto Morandotti, Arnan Mitchell, Kun Xu, and David J. Moss, "Neuromorphic computing based on wavelength-division

- multiplexing", *IEEE Journal of Selected Topics in Quantum Electronics* **29** (2) 7400112 (2023). DOI:10.1109/JSTQE.2022.3203159.
84. Yunping Bai, Xingyuan Xu, Mengxi Tan, Yang Sun, Yang Li, Jiayang Wu, Roberto Morandotti, Arnan Mitchell, Kun Xu, and David J. Moss, "Photonic multiplexing techniques for neuromorphic computing", *Nanophotonics* vol. 12 (5): 795–817 (2023). DOI:10.1515/nanoph-2022-0485.
 85. Chawaphon Prayoonpong, Andreas Boes, Xingyuan Xu, Mengxi Tan, Sai T. Chu, Brent E. Little, Roberto Morandotti, Arnan Mitchell, David J. Moss, and Bill Corcoran, "Frequency comb distillation for optical superchannel transmission", *Journal of Lightwave Technology* vol. 39 (23) 7383-7392 (2021). DOI: 10.1109/JLT.2021.3116614.
 86. Mengxi Tan, Xingyuan Xu, Jiayang Wu, Bill Corcoran, Andreas Boes, Thach G. Nguyen, Sai T. Chu, Brent E. Little, Roberto Morandotti, Arnan Mitchell, and David J. Moss, "Integral order photonic RF signal processors based on a soliton crystal micro-comb source", *IOP Journal of Optics* vol. 23 (11) 125701 (2021). <https://doi.org/10.1088/2040-8986/ac2eab>
 87. Yang Sun, Jiayang Wu, Yang Li, Xingyuan Xu, Guanghui Ren, Mengxi Tan, Sai Tak Chu, Brent E. Little, Roberto Morandotti, Arnan Mitchell, and David J. Moss, "Optimizing the performance of microcomb based microwave photonic transversal signal processors", *Journal of Lightwave Technology* vol. 41 (23) pp 7223-7237 (2023). DOI: 10.1109/JLT.2023.3314526.
 88. Mengxi Tan, Xingyuan Xu, Andreas Boes, Bill Corcoran, Thach G. Nguyen, Sai T. Chu, Brent E. Little, Roberto Morandotti, Jiayang Wu, Arnan Mitchell, and David J. Moss, "Photonic signal processor for real-time video image processing based on a Kerr microcomb", *Communications Engineering* vol. 2 94 (2023). DOI:10.1038/s44172-023-00135-7
 89. Mengxi Tan, Xingyuan Xu, Jiayang Wu, Roberto Morandotti, Arnan Mitchell, and David J. Moss, "Photonic RF and microwave filters based on 49GHz and 200GHz Kerr microcombs", *Optics Communications*, vol. 465, Article: 125563 (2020). doi:10.1016/j.optcom.2020.125563. doi.org/10.1063/1.5136270.
 90. Yang Sun, Jiayang Wu, Yang Li, Mengxi Tan, Xingyuan Xu, Sai Chu, Brent Little, Roberto Morandotti, Arnan Mitchell, and David J. Moss, "Quantifying the Accuracy of Microcomb-based Photonic RF Transversal Signal Processors", *IEEE Journal of Selected Topics in Quantum Electronics* vol. 29 no. 6, pp. 1-17, Art no. 7500317 (2023). 10.1109/JSTQE.2023.3266276.
 91. Yang Li, Yang Sun, Jiayang Wu, Guanghui Ren, Bill Corcoran, Xingyuan Xu, Sai T. Chu, Brent E. Little, Roberto Morandotti, Arnan Mitchell, and David J. Moss, "Processing accuracy of microcomb-based microwave photonic signal processors for different input signal waveforms", *MDPI Photonics* **10**, 10111283 (2023). DOI:10.3390/photonics10111283
 92. Caitlin E. Murray, Mengxi Tan, Chawaphon Prayoonpong, Sai T. Chu, Brent E. Little, Roberto Morandotti, Arnan Mitchell, David J. Moss and Bill Corcoran, "Investigating the thermal robustness of soliton crystal microcombs", *Optics Express* **31**(23), 37749-37762 (2023).
 93. Yang Sun, Jiayang Wu, Yang Li, and David J. Moss, "Comparison of microcomb-based RF photonic transversal signal processors implemented with discrete components versus integrated chips", *MDPI Micromachines* **14**, 1794 (2023). <https://doi.org/10.3390/mi14091794>
 94. W. Bogaerts, P. De Heyn, T. Van Vaerenbergh, K. De Vos, S. Kumar Selvaraja, T. Claes, P. Dumon, P. Bienstman, D. Van Thourhout, and R. Baets, "Silicon microring resonators," *Laser & Photonics Reviews*, vol. 6, no. 1, pp. 47-73, 2012.
 95. L. Chrostowski, and M. Hochberg, *Silicon photonics design: from devices to systems*: Cambridge University Press, 2015.
 96. Y. Qu, J. Wu, Y. Zhang, Y. Yang, L. Jia, H. E. Dirani, S. Kerdiles, C. Sciancalepore, P. Demongodin, C. Grillet, C. Monat, B. Jia, and D. J. Moss, "Integrated optical parametric amplifiers in silicon nitride waveguides incorporated with 2D graphene oxide films," *Light: Advanced Manufacturing*, vol. 4, no. 4, pp. 1, 2023.
 97. Wu, J. et al. "2D layered graphene oxide films integrated with micro-ring resonators for enhanced nonlinear optics", *Small* Vol. 16, 1906563 (2020).
 98. Wu, J. et al., "Graphene oxide waveguide and micro-ring resonator polarizers", *Laser and Photonics Reviews* Vol. 13, 1900056 (2019).
 99. Zhang, Y. et al., "Enhanced Kerr nonlinearity and nonlinear figure of merit in silicon nanowires integrated with 2d graphene oxide films", *ACS Applied Material Interfaces* Vol. 12, 33094-33103 (2020).
 100. Qu, Y. et al., "Enhanced four-wave mixing in silicon nitride waveguides integrated with 2d layered graphene oxide films", *Advanced Optical Materials* Vol. 8, 2001048 (2020).
 101. Yuning Zhang, Jiayang Wu, Yunyi Yang, Yang Qu, Linnan Jia, Houssein El Dirani, Sébastien Kerdiles, Corrado Sciancalepore, Pierre Demongodin, Christian Grillet, Christelle Monat, Baohua Jia, and David J. Moss, "Enhanced supercontinuum generated in SiN waveguides coated with GO films", *Advanced Materials Technologies* **8** (1) 2201796 (2023). DOI:10.1002/admt.202201796.
 102. Yuning Zhang, Jiayang Wu, Linnan Jia, Yang Qu, Baohua Jia, and David J. Moss, "Graphene oxide for nonlinear integrated photonics", *Laser and Photonics Reviews* **17** 2200512 (2023). DOI:10.1002/lpor.202200512.

103. Jiayang Wu, H.Lin, David J. Moss, T.K. Loh, Baohua Jia, "Graphene oxide for electronics, photonics, and optoelectronics", *Nature Reviews Chemistry* 7 (3) 162–183 (2023). doi.org/10.1038/s41570-022-00458-7.
104. Yang Qu, Jiayang Wu, Yuning Zhang, Yunyi Yang, Linnan Jia, Baohua Jia, and David J. Moss, "Photo thermal tuning in GO-coated integrated waveguides", *Micromachines* Vol. 13 1194 (2022). doi.org/10.3390/mi13081194
105. Yuning Zhang, Jiayang Wu, Yunyi Yang, Yang Qu, Houssein El Dirani, Romain Crochemore, Corrado Sciancalepore, Pierre Demongodin, Christian Grillet, Christelle Monat, Baohua Jia, and David J. Moss, "Enhanced self-phase modulation in silicon nitride waveguides integrated with 2D graphene oxide films", *IEEE Journal of Selected Topics in Quantum Electronics* Vol. 29 (1) 5100413 (2023). DOI: 10.1109/JSTQE.2022.3177385
106. Yuning Zhang, Jiayang Wu, Yunyi Yang, Yang Qu, Linnan Jia, Baohua Jia, and David J. Moss, "Enhanced spectral broadening of femtosecond optical pulses in silicon nanowires integrated with 2D graphene oxide films", *Micromachines* Vol. 13 756 (2022). DOI:10.3390/mi13050756.
107. Jiayang Wu, Yuning Zhang, Junkai Hu, Yunyi Yang, Di Jin, Wenbo Liu, Duan Huang, Baohua Jia, David J. Moss, "Novel functionality with 2D graphene oxide films integrated on silicon photonic chips", *Advanced Materials* Vol. 36 2403659 (2024). DOI: 10.1002/adma.202403659.
108. Di Jin, Jiayang Wu, Junkai Hu, Wenbo Liu, Yuning Zhang, Yunyi Yang, Linnan Jia, Duan Huang, Baohua Jia, and David J. Moss, "Silicon photonic waveguide and microring resonator polarizers incorporating 2D graphene oxide films", *Applied Physics Letters* vol. 125, 000000 (2024); doi: 10.1063/5.0221793.
109. Yuning Zhang, Jiayang Wu, Linnan Jia, Di Jin, Baohua Jia, Xiaoyong Hu, David Moss, Qihuang Gong, "Advanced optical polarizers based on 2D materials", *npj Nanophotonics* Vol. 1, (2024). DOI: 10.1038/s44310-024-00028-3.
110. Junkai Hu, Jiayang Wu, Wenbo Liu, Di Jin, Houssein El Dirani, Sébastien Kerdiles, Corrado Sciancalepore, Pierre Demongodin, Christian Grillet, Christelle Monat, Duan Huang, Baohua Jia, and David J. Moss, "2D graphene oxide: a versatile thermo-optic material", *Advanced Functional Materials* 34 2406799 (2024). DOI: 10.1002/adfm.202406799.
111. Yang Qu, Jiayang Wu, Yuning Zhang, Yunyi Yang, Linnan Jia, Houssein El Dirani, Sébastien Kerdiles, Corrado Sciancalepore, Pierre Demongodin, Christian Grillet, Christelle Monat, Baohua Jia, and David J. Moss, "Integrated optical parametric amplifiers in silicon nitride waveguides incorporated with 2D graphene oxide films", *Light: Advanced Manufacturing* 4 39 (2023). https://doi.org/10.37188/lam.2023.039.
112. Di Jin, Wenbo Liu, Linnan Jia, Junkai Hu, Duan Huang, Jiayang Wu, Baohua Jia, and David J. Moss, "Thickness and Wavelength Dependent Nonlinear Optical Absorption in 2D Layered MXene Films", *Small Science* 4 2400179 (2024). DOI:10.1002/smsc202400179;
113. Linnan Jia, Jiayang Wu, Yuning Zhang, Yang Qu, Baohua Jia, Zhigang Chen, and David J. Moss, "Fabrication Technologies for the On-Chip Integration of 2D Materials", *Small: Methods* Vol. 6, 2101435 (2022). DOI:10.1002/smt.202101435.
114. Yuning Zhang, Jiayang Wu, Yang Qu, Linnan Jia, Baohua Jia, and David J. Moss, "Design and optimization of four-wave mixing in microring resonators integrated with 2D graphene oxide films", *Journal of Lightwave Technology* Vol. 39 (20) 6553–6562 (2021). DOI:10.1109/JLT.2021.3101292.
115. Yuning Zhang, Jiayang Wu, Yang Qu, Linnan Jia, Baohua Jia, and David J. Moss, "Optimizing the Kerr nonlinear optical performance of silicon waveguides integrated with 2D graphene oxide films", *Journal of Lightwave Technology* Vol. 39 (14) 4671–4683 (2021). DOI: 10.1109/JLT.2021.3069733.
116. Yang Qu, Jiayang Wu, Yuning Zhang, Yao Liang, Baohua Jia, and David J. Moss, "Analysis of four-wave mixing in silicon nitride waveguides integrated with 2D layered graphene oxide films", *Journal of Lightwave Technology* Vol. 39 (9) 2902–2910 (2021). DOI: 10.1109/JLT.2021.3059721.
117. Jiayang Wu, Linnan Jia, Yuning Zhang, Yang Qu, Baohua Jia, and David J. Moss, "Graphene oxide: versatile films for flat optics to nonlinear photonic chips", *Advanced Materials* Vol. 33 (3) 2006415, pp.1-29 (2021). DOI:10.1002/adma.202006415.
118. Y. Qu, J. Wu, Y. Zhang, L. Jia, Y. Yang, X. Xu, S. T. Chu, B. E. Little, R. Morandotti, B. Jia, and D. J. Moss, "Graphene oxide for enhanced optical nonlinear performance in CMOS compatible integrated devices", Paper No. 11688-30, PW21O-OE109-36, 2D Photonic Materials and Devices IV, SPIE Photonics West, San Francisco CA March 6-11 (2021). doi.org/10.1117/12.2583978
119. Yang Qu, Jiayang Wu, Yunyi Yang, Yuning Zhang, Yao Liang, Houssein El Dirani, Romain Crochemore, Pierre Demongodin, Corrado Sciancalepore, Christian Grillet, Christelle Monat, Baohua Jia, and David J. Moss, "Enhanced nonlinear four-wave mixing in silicon nitride waveguides integrated with 2D layered graphene oxide films", *Advanced Optical Materials* vol. 8 (21) 2001048 (2020). DOI: 10.1002/adom.202001048. arXiv:2006.14944.
120. Yuning Zhang, Yang Qu, Jiayang Wu, Linnan Jia, Yunyi Yang, Xingyuan Xu, Baohua Jia, and David J. Moss, "Enhanced Kerr nonlinearity and nonlinear figure of merit in silicon nanowires integrated with 2D graphene oxide films", *ACS Applied Materials and Interfaces* vol. 12 (29) 33094–33103 June 29 (2020). DOI:10.1021/acami.0c07852

121. Jiayang Wu, Yunyi Yang, Yang Qu, Yuning Zhang, Linnan Jia, Xingyuan Xu, Sai T. Chu, Brent E. Little, Roberto Morandotti, Baohua Jia, and David J. Moss, "Enhanced nonlinear four-wave mixing in microring resonators integrated with layered graphene oxide films", *Small* vol. 16 (16) 1906563 (2020). DOI: 10.1002/sml.201906563
122. Jiayang Wu, Yunyi Yang, Yang Qu, Xingyuan Xu, Yao Liang, Sai T. Chu, Brent E. Little, Roberto Morandotti, Baohua Jia, and David J. Moss, "Graphene oxide waveguide polarizers and polarization selective micro-ring resonators", Paper 11282-29, SPIE Photonics West, San Francisco, CA, 4 - 7 February (2020). doi: 10.1117/12.2544584
123. Jiayang Wu, Yunyi Yang, Yang Qu, Xingyuan Xu, Yao Liang, Sai T. Chu, Brent E. Little, Roberto Morandotti, Baohua Jia, and David J. Moss, "Graphene oxide waveguide polarizers and polarization selective micro-ring resonators", *Laser and Photonics Reviews* vol. 13 (9) 1900056 (2019). DOI:10.1002/lpor.201900056.
124. Yunyi Yang, Jiayang Wu, Xingyuan Xu, Sai T. Chu, Brent E. Little, Roberto Morandotti, Baohua Jia, and David J. Moss, "Enhanced four-wave mixing in graphene oxide coated waveguides", *Applied Physics Letters Photonics* vol. 3 120803 (2018). doi: 10.1063/1.5045509.
125. Linnan Jia, Yang Qu, Jiayang Wu, Yuning Zhang, Yunyi Yang, Baohua Jia, and David J. Moss, "Third-order optical nonlinearities of 2D materials at telecommunications wavelengths", *Micromachines (MDPI)*, 14, 307 (2023). <https://doi.org/10.3390/mi14020307>.
126. Linnan Jia, Dandan Cui, Jiayang Wu, Haifeng Feng, Tieshan Yang, Yunyi Yang, Yi Du, Weichang Hao, Baohua Jia, David J. Moss, "BiOBr nanoflakes with strong nonlinear optical properties towards hybrid integrated photonic devices", *Applied Physics Letters Photonics* vol. 4 090802 vol. (2019). DOI: 10.1063/1.5116621
127. Linnan Jia, Jiayang Wu, Yunyi Yang, Yi Du, Baohua Jia, David J. Moss, "Large Third-Order Optical Kerr Nonlinearity in Nanometer-Thick PdSe₂ 2D Dichalcogenide Films: Implications for Nonlinear Photonic Devices", *ACS Applied Nano Materials* vol. 3 (7) 6876–6883 (2020). DOI:10.1021/acsnm.0c01239.
128. D. Jin, W. Liu, L. Jia, Y. Zhang, J. Hu, H. El Dirani, S. Kerdiles, C. Sciancalepore, P. Demongodin, C. Grillet, C. Monat, D. Huang, J. Wu, B. Jia, and D. J. Moss, "Thickness- and wavelength-dependent nonlinear optical absorption in 2D layered MXene films," *Small Science*, vol. n/a, no. n/a, pp. 2400179.

Disclaimer/Publisher's Note: The statements, opinions and data contained in all publications are solely those of the individual author(s) and contributor(s) and not of MDPI and/or the editor(s). MDPI and/or the editor(s) disclaim responsibility for any injury to people or property resulting from any ideas, methods, instructions or products referred to in the content.